Nonlinear convective/absolute instabilities in parallel two-dimensional wakes

Ivan Delbende and Jean-Marc Chomaz
LadHyX, CNRS-UMR 7646, École Polytechnique, 91128 Palaiseau Cedex, France

The linear versus nonlinear convective/absolute instability of a family of plane wake profiles at low Reynolds number is investigated by numerically comparing the linearized and the fully nonlinear impulse responses. Through an analysis of the linear flow response obtained by direct numerical simulation (DNS), the linear temporal and spatiotemporal instability properties are retrieved, in excellent agreement with the properties obtained by Monkewitz [Phys. Fluids **31**, 3000 (1994)] from the study of the associated viscous dispersion relation. Nonlinear terms are then shown to limit the amplitude to a saturation level within the response wave packet, while leaving the trailing and leading edges unaffected. For this family of open shear flows, the velocities of the fronts, formed between the trailing or leading edge and the central saturated region, are thus selected according to the linear Dee and Langer criterion [Phys. Rev. Lett. **50**, 383 (1983)], whereas the front solutions are fully nonlinear. This property may be of importance in justifying the use of *linear* instability properties to predict the onset and the frequency of the von Kármán vortex street, as determined by Hammond and Redekopp [J. Fluid Mech. **331**, 231 (1997)]. © *1998 American Institute of Physics.* [S1070-6631(98)01710-3]

I. INTRODUCTION

Front propagation in spatially extended systems occurs whenever two states with different stability properties coexist in contiguous spatial domains. The associated pattern selection problem is then tantamount to the determination of the behavior of the front separating these two domains. Front selection has been recently investigated in Taylor–Couette[1] and Rayleigh–Bénard[2] systems with small throughflow from a weakly nonlinear point of view. Our goal in the present study is to extend these investigations to highly unstable open shear flows where fully nonlinear effects are predominant, in order to discriminate between linear and purely nonlinear mechanisms for the spreading of the saturated state. The study is conducted in the context of plane parallel wake flows, where the determination of the front-selection mechanism is of great importance in predicting the critical threshold and the characteristics of the von Kármán vortex street.

Open shear flows such as heated or low-density jets[3,4] and bluffbody wakes[5] are known to sustain self-excited oscillations in a certain range of parameters. This resonance phenomenon is now commonly described by resorting to the concepts of linear convective/absolute instabilities and global modes.[6] The most celebrated example of such a behavior is provided by vortex shedding past two-dimensional bluff bodies: the flow distortion induced by the presence of a cylinder in the flow gives rise to the so-called Bénard–Kármán vortex street as soon as the Reynolds number $Re^{(D)}$ based on diameter and free-stream velocity exceeds the critical value $Re_G^{(D)} \sim 47$.

This spectacular phenomenon has been ascribed by Mathis, Provansal, and Boyer[5] to a supercritical Hopf bifurcation toward a limit cycle. Since then, many attempts have been made to link this global description to the local insta-

bility properties at each streamwise location. Monkewitz[7] has determined the convective/absolute nature of the instability for a family of profiles with different shear layer thicknesses [see Eq. (2)] pertinent to the description of bluffbody wakes. Through a careful fit of experimental data measured at the location of greatest reverse flow intensity, he was able to describe the qualitative changes that occur as the Reynolds number $Re^{(D)}$ is increased from zero. As summarized in Fig. 1, a transition from local stability to convective instability first occurs at $Re^{(D)} \sim 5$, then from convective to absolute instability at $Re^{(D)} \sim 25$. However, the latter transition has no experimental trace, as it is based on a fictitious parallel underlying basic flow.[6] The global bifurcation toward Kármán vortex shedding eventually takes place at $Re^{(D)} \sim 47$. This vision is corroborated by the numerical study of Hannemann and Örtel.[8] These authors simulated the basic wake flow and determined the local instability properties in order to discriminate between the shedding-frequency selection criteria proposed by several investigators.[9–11] It was found that a substantial region of the near wake is absolutely unstable at the onset of vortex shedding. The finding is qualitatively consistent with the model studies by Chomaz, Huerre, and Redekopp,[12] Le Dizès *et al.*,[13] and Pier *et al.*:[14] absolute instability is a prerequisite for the occurrence of global oscillations, but it is not sufficient. This explains why the global instability threshold is usually located at higher control parameter values than the local instability threshold (Fig. 1).

Above the onset of vortex shedding, the growth of the global mode is well described by a Stuart–Landau model, as supported by the experiments of Provansal, Mathis and Boyer[5] and Schumm, Berger, and Monkewitz:[15] the weakly nonlinear formalism appears to faithfully describe the wake dynamics even ''unreasonably'' [15] far above the global instability threshold for values of the bifurcation parameter
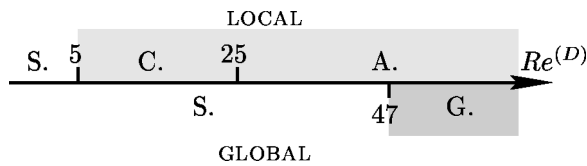
FIG. 1. Local versus global instability properties of the two-dimensional cylinder wake. S: stable, C: existence of a convective instability pocket, A: existence of an absolute instability pocket, G: globally unstable. Grey areas denote instability.

$(\mathrm{Re}^{(D)} - \mathrm{Re}_G^{(D)})/\mathrm{Re}^{(D)}$ of order unity. More recently, Hammond and Redekopp[16] systematically investigated symmetric and asymmetric wakes past a blunt edged plate with or without blowing and suction. The properties of vortex shedding were predicted accurately via a numerical approach within the framework of the weakly nonparallel[17] approximation: the mean flow was obtained by direct numerical simulation and the local linear instability properties were determined at each downstream location X. The values of the linear growth rate and shedding frequency were determined by analytic continuation in the complex X plane at the dominant saddle point of the complex absolute frequency $\omega_0(X)$.

That linear theory accounts so well for the wake dynamics is surprising for two main reasons. First, the flow is strongly nonparallel and the commonly used WKBJ approximation may legitimately be questioned. Second, the flow near global instability onset is highly unstable in a substantial region of the wake as a result of the gap existing between local and global instability thresholds (Fig. 1): nonlinear effects are thus already strong when $\mathrm{Re}^{(D)}$ is close to $\mathrm{Re}_G^{(D)}$, as illustrated on Fig. 2 in the context of the cylinder-wake ex-

periment performed by Le Gal and Croquette.[18] In the subcritical regime, a small perturbation of the cylinder causes a wavepacket to grow, form a saturated vortex street which is ultimately advected downstream, as the system is below the global instability threshold. The passive tracer is strongly and rapidly displaced, indicating the presence of strongly nonlinear effects linked to the high local instability in the near-wake.

When strong nonlinearities intervene, linear convective/absolute instability concepts should *a priori* be replaced by their nonlinear counterparts.[19] Both linear and nonlinear theories are outlined below.

Linear spatio-temporal instability properties are based on the behavior of the linear impulse response of the flow in a given reference frame. If the flow is unstable, any localized pulse develops along the x (streamwise) direction into a wave packet of spatio-temporal modes which grow exponentially along some rays $x/t = v$ and decay along other rays. In most situations, the unstable modes are delineated by a pair of particular rays $x/t = v_\pm$ or ''edges'' along which neutral waves propagate. The knowledge of the edge velocities $v_\pm$ allows us to discriminate between convective and absolute instabilities (see Huerre and Monkewitz[6] for a review). If v_- and v_+ have the same sign (say positive), the linear response decays at each fixed location, indicating a convective type of instability. If by contrast v_- is negative and v_+ is positive, the spatio-temporal ray $x/t = 0$ lies in the range of exponentially growing modes, which indicates an absolute type of instability.

The extension of these concepts to the nonlinear régime[19] involves the evolution of localized perturbations of
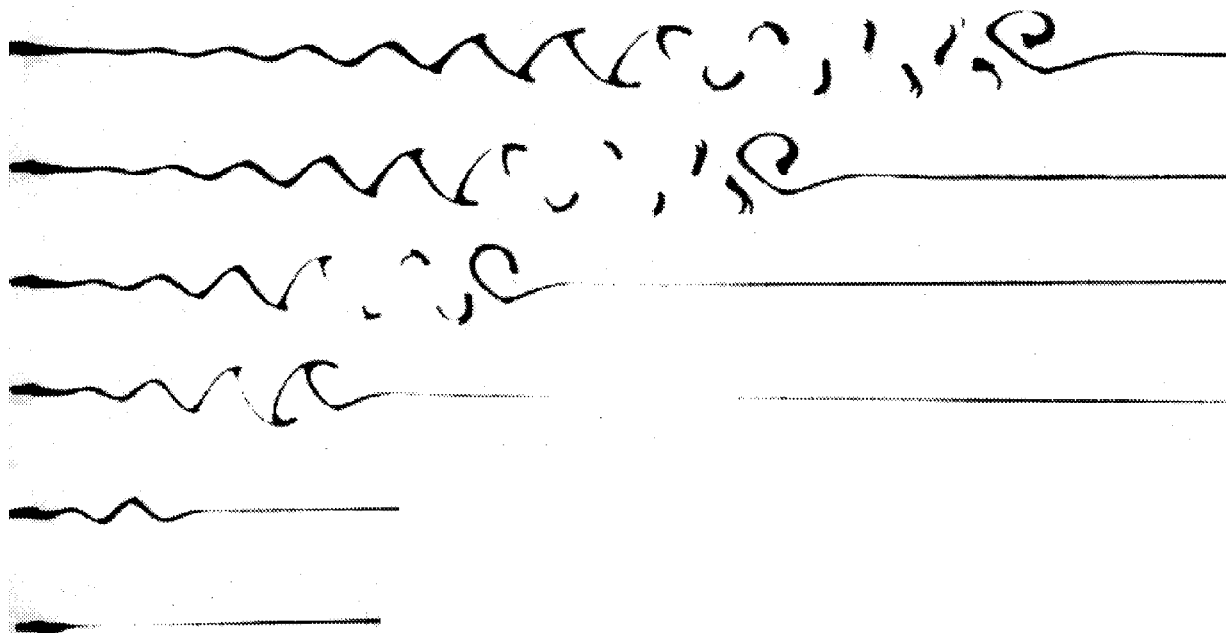

FIG. 2. Streakline of a passive tracer visualizing the impulse response in a cylinder wake at several times. In this waterfall presentation of an experiment by Le Gal and Croquette,[18] time is running from the bottom to the top picture by regular step increases. The Reynolds number $\mathrm{Re}^{(D)} = 35$ is subcritical, but local instability causes a finite-amplitude wave packet to develop in space and time. The passive scalar is strongly and rapidly displaced. Courtesy of Le Gal and Croquette.
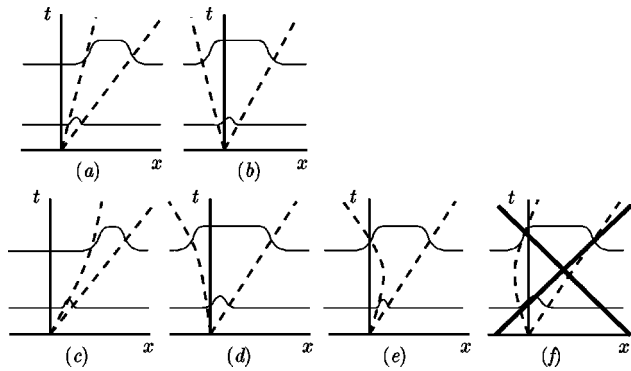
FIG. 3. Typical impulse responses of a homogeneous medium illustrating (a)–(b) linear and (c)–(f) nonlinear velocity selection. In cases (a)–(d), the convective/absolute nature of the flow is preserved from the linear to nonlinear régime [convective for (a) and (c), absolute for (b) and (d)]. By contrast, case (e) illustrates linearly convective and nonlinearly absolute instability. The reverse (f), linearly absolute and nonlinearly convective instability, is impossible.

finite amplitude. The generated wave packets may then be bounded by two fronts of fixed shape propagating at velocities $v_\pm^{NL}$. By analogy with the linear case, the instability is nonlinearly absolute if a wave packet exists for which v_-^{NL} and v_+^{NL} have opposite signs. Otherwise, it is nonlinearly convective.

The relation between linear and nonlinear convective/absolute instability notions is nontrivial and can be associated with the concept of front-velocity selection, which has been extensively studied in the past decade.[20–22] Consider a small-amplitude perturbation initially localized within an unstable medium (Fig. 3). Initially, the disturbance grows according to linear instability theory, and its edges propagate at the linearly selected velocities $v_\pm$. As the exponential growth becomes compensated by nonlinear terms, the wave packet saturates while the linear edges transform into nonlinear fronts. Dee and Langer[23] have proposed a "marginal stability" mechanism, also interpreted as a dynamical process for linear front-velocity selection by van Saarloos,[21] in which the fronts of the nonlinear wave packet simply propagate at the same speed as the linear precursor edges ($v_\pm^{NL} = v_\pm$), as sketched in Figs. 3(a) and 3(b). This mechanism is based on the assumption that the infinitesimal perturbations preceding the front necessarily comply with the linear dispersion relation and dictate the entire front dynamics. Nevertheless, in some situations, the wave packet saturation causes a different front with higher velocity to emerge, as shown by van Saarloos.[22] The selection is then said to be *nonlinear*, as it is imposed by the nonlinear saturated region. In the case of nonlinear velocity selection, which may *a priori* occur for the leading and/or the trailing front, the nonlinearly selected front velocity $v_\pm^{NL}$ necessarily lies outside the range of velocities $[v_-, v_+]$, (i.e., $v_-^{NL} < v_-$ and/or $v_+^{NL} > v_+$), as sketched in Figs. 3(c)–3(e). Otherwise, a linear front could emerge and propagate at the linear edge velocity $v_\pm$. This property implies, in particular, that the flow may be linearly convectively unstable ($v_- > 0$) and nonlinearly absolute unstable ($v_-^{NL} < 0$) [Fig. 3(e)]. In such a situation, the flow may bifurcate toward another state such as a limit cycle,

although it is linearly convectively unstable. Note also that, since the nonlinear wave packet contains the linear wave packet, linear absolute instability necessarily implies nonlinear absolute instability, which, for instance, forbids the scenario sketched in Fig. 3(f).

The above notions have found an illustration in Taylor–Couette[1] and Rayleigh–Bénard[2] experiments in open flow configurations. The stream forced in the axial[1] or horizontal[2] direction, normal to the primary instability rolls (Ref. 1 accounts for a two-dimensional simulation while in Ref. 2 experimental results are reported). In both instances, the front selection was observed to be linear. These findings justify the use of linear criteria in the prediction of resonance in such systems.

However, it should be noted that in the above studies,[1,2] the superimposed throughflow is small and that the behavior may thus be described in a weakly nonlinear framework by a Ginzburg–Landau amplitude equation. The validity of linear criteria for front selection is therefore not surprising. By contrast, shear flows such as bluffbody wakes present local instability growth rates of order unity, as advection and shear cannot be monitored independently. Their behavior should *a priori* be affected by strongly nonlinear effects, since at the threshold, the wave packet amplitude is also of order unity. It is hence worth examining the existence of fronts separating the basic unstable state from the saturated bifurcated stable state, and also investigating the influence of *strong nonlinearities* on front-velocity selection in *open shear flows*. Such a study is undertaken here in the context of two-dimensional symmetric parallel wake profiles introduced by Monkewitz and Nguyen.[11] The strong nonparallelism of realistic bluffbody wake flows is deliberately ignored, since we wish to focus on the effects of nonlinear terms. We find that, for the selected family of wake profiles, front selection is governed by linear mechanisms. It should be emphasized that linear front-velocity selection is *no* generic feature of nonlinear media and that nonlinear selection has been observed in other experimental situations, such as chemically reacting systems[24] and liquid crystals.[25]

This paper is organized as follows. The numerical aspects of the simulation as well as investigation techniques are presented in Sec. II. Linear temporal and spatiotemporal properties are retrieved from DNS in Sec. III for two different wake configurations: a strongly confined periodic wake and a weakly confined wake. The nonlinear wave packet evolution in both configurations is presented in Sec. IV. Conclusions regarding the validity of linear theory at the global instability threshold are discussed in Sec. V.

II. NUMERICAL ASPECTS

A. Direct numerical simulation technique

In all the following, the basic wake is assumed parallel in the streamwise x direction, and the streamwise velocity component U depends solely on the cross-stream coordinate y. The wake half-width $D/2$ and the free-stream velocity U_∞ are used to make distances and velocities dimensionless. Let $\mathbf{U} = U(y)\hat{\mathbf{x}}$ and $\mathbf{\Omega} = \nabla \times \mathbf{U}$ denote the velocity and vorticity of the basic flow. The evolution of velocity ($\mathbf{u}$), vorticity ($\boldsymbol{\omega}$),

Phys. Fluids, Vol. 10, No. 11, November 1998

I. Delbende and J.-M. Chomaz   2727

and pressure (p) disturbances is governed by the incompressible two-dimensional Navier–Stokes equations written here in velocity/vorticity formulation:

$$\frac{\partial \mathbf{u}}{\partial t} = \mathbf{u} \times \mathbf{\Omega} + \mathbf{U} \times \boldsymbol{\omega} + \mathbf{u} \times \boldsymbol{\omega} + \boldsymbol{\nabla}\left[p + \mathbf{u} \cdot \mathbf{U} + \frac{\mathbf{u}^2}{2}\right]$$

$$+ \frac{1}{\mathrm{Re}} \, \boldsymbol{\nabla}^2 \mathbf{u}, \tag{1}$$

where Re designates the Reynolds number based on the above reference scales (the correspondence $\mathrm{Re} = \mathrm{Re}^{(D)}/2$ holds). Note that the diffusion acting on the basic flow is assumed to be compensated by a body force and that the corresponding term $\mathrm{Re}^{-1} \boldsymbol{\nabla}^2 \mathbf{U}$ has thus been removed in (1), as is often done in theoretical studies in order to make the problem autonomous. In particular, it allows direct comparisons with the alternative branch-point analysis by Monkewitz,[7] which relies on the same assumptions. The numerical procedure here consists of a pseudospectral code originally written by Vincent and Meneguzzi,[26] adapted, optimized, and validated by Brancher[27] to two-dimensional rectangular domains. Details on the numerical technique can be found in Ref. 28. The Fourier formulation enforces periodicity of the system along both the streamwise x and the cross-stream y directions. Collocation points are distant by $\delta x = \delta y = 0.1$. The physical domain made up of 1024 or 2048 points along x is chosen long enough to ensure that the perturbation remains localized far away from the streamwise boundaries during the total simulation time and that the results are indeed unaffected by streamwise periodicity. In the following, two different cross-stream box widths are successively adopted. For the first one, $L_y = 4.8$, the wake is strongly confined between two adjacent (identical) wakes situated 2.4 diameters apart. For the second one, $L_y = 25.6$, the domain is wide enough, so that the computed solutions satisfactorily approximate the dynamics of a single wake in an infinite medium.

The basic wake profile adopted here has been elaborated by Monkewitz and Nguyen.[11] The streamwise component of velocity is given by

$$U(y) = 1 - \Lambda + 2\Lambda \, \frac{1}{1 + \sinh^{2N}|y \, \sinh^{-1}(1)|}, \quad \text{with} \;\; N = 2. \tag{2}$$

Since the centerline velocity U_0 is chosen to be zero, the velocity ratio $\Lambda \equiv (U_0 - U_\infty)/(U_0 + U_\infty)$ is $\Lambda = -1$ throughout the study. Results for other Λ values can be obtained by Galilean transformation. For the selected value of N, each vorticity layer is (well) sampled on ten mesh lines approximately. This wake profile has also been considered by Delfs et al.,[29] who used a vortex blob method to simulate the inviscid and viscous response to a localized pulse for different values of the velocity ratio Λ.

The computational field is initialized by the divergence-free velocity disturbance $\mathbf{u}(x,y,t=0)$ with components:

$$u_x = -(y - y_0)\exp\left[-\left(\frac{x^2}{2\sigma_x^2} + \frac{(y-y_0)^2}{2\sigma_y^2}\right)\right], \tag{3}$$

$$u_y = \frac{\sigma_y^2}{\sigma_x^2} \, x \, \exp\left[-\left(\frac{x^2}{2\sigma_x^2} + \frac{(y-y_0)^2}{2\sigma_y^2}\right)\right].$$

The initial perturbation takes the form of a small vorticity spot located at ($x = 0$, $y = y_0$). The distribution envelope is Gaussian and has a typical extent σ_x along the x direction and σ_y along the y direction. The length scales σ_x and σ_y must a priori be taken as small as possible, as the initial conditions should take the form of a delta function. Nevertheless, the values $\sigma_x = 0.4$, $\sigma_y = 0.6$ have been chosen in order to ensure satisfactory sampling in the truncated spectral space. In this manner, the initial perturbation at least contains all the physically relevant wave numbers, as checked a posteriori. Moreover, it is centered at $y_0 = 0.5$ in one of the two wake shear layers, so that no particular symmetry is enforced on the solution by the initial conditions.

B. Decomposition procedure for linear simulations

A set of *linear* simulations is first performed whereby the linear instability properties of the basic flow under investigation can be derived. The evolution of an initially localized perturbation is simulated according to the Navier–Stokes equation linearized in the vicinity of the basic state, i.e., Eq. (1), in which the terms $\mathbf{u} \times \boldsymbol{\omega}$ and $\boldsymbol{\nabla}\mathbf{u}^2 2$ are omitted. Through the analysis of the simulated wave packet described below, the linear temporal and spatiotemporal instability properties are retrieved.

The theoretical treatment of the associated Orr–Sommerfeld eigenvalue problem[30] associated with the symmetric velocity profile (2) reveals the existence of a discrete set of branches parametrized by the streamwise wave number k. They pertain either to varicose modes for which the vorticity eigenfunction is symmetric with respect to the x axis, or to sinuous modes, for which the vorticity eigenfunction is antisymmetric. The contributions ω_{sin} and ω_{var}, of sinuous and varicose modes, respectively, to the perturbation vorticity ω can be separated easily by considering the even and odd components of ω:

$$\omega_{\mathrm{sin}}(x,y,t) = \tfrac{1}{2}[\omega(x,y,t) + \omega(x,-y,t)], \tag{4}$$

$$\omega_{\mathrm{var}}(x,y,t) = \tfrac{1}{2}[\omega(x,y,t) - \omega(x,-y,t)]. \tag{5}$$

Each contribution can then be considered independently. The procedure is detailed below for the sinuous part, but the same holds for the varicose part.

1. Temporal instability, analysis in spectral space

In the temporal formulation of instability problems, a *real* wave number k in the x direction is prescribed and the corresponding complex frequency $\omega_{\mathrm{sin}}(k)$ is sought. As explained in Brancher,[27] the simulation of an initially localized impulse generates a wave packet with a broad spectrum structure (see, for instance, Fig. 4). By considering the evolution of the spectrum in time, one may recover in a single run the leading temporal instability properties of the basic flow prevailing for each streamwise wave number k.

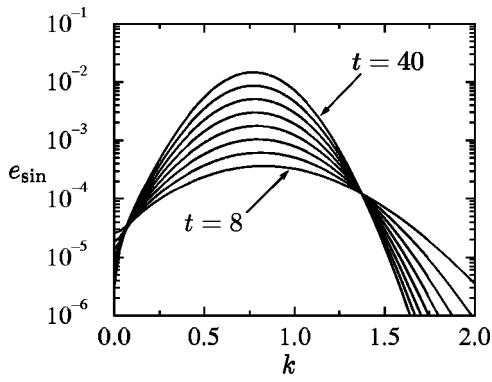The procedure is applied here on the perturbation-enstrophy spectrum:

FIG. 4. Perturbation spectrum $e_{\sin}$ of the dominant sinuous mode as a function of real streamwise wave number k. The curves are extracted from the simulated wake impulse response at several times $t=8,12,...,40$ for Re $=20$ and $L_y=4.8$.

$$e_{\sin}(k,t)=\left(\int_0^{+\infty}|\hat{\omega}_{\sin}(k,y,t)|^2 \, dy\right)^{1/2}, \tag{6}$$

which measures the amplitude of the temporal wave under consideration. According to temporal instability theory, the above variable is known to evolve asymptotically for large times as

$$e_{\sin}(k,t)\propto e^{\omega_{i,\sin}(k)t}, \quad t\to\infty, \tag{7}$$

where $\omega_{i,\sin}(k)$ denotes the leading temporal growth rate at wave number k. Conversely, $\omega_{i,\sin}(k)$ can be expressed as

$$\omega_{i,\sin}(k)\sim\frac{\partial}{\partial t}\ln e_{\sin}(k,t), \quad t\to\infty. \tag{8}$$

If $\omega_{i,\sin}(k)$ is well separated from the other eigenvalues of a smaller growth rate, it is possible to obtain its value from the computed spectrum distribution $e_{\sin}(k,t)$ for large times, by making use of the discretized form of (8):

$$\omega_{i,\sin}(k)\approx\frac{\ln[e_{\sin}(k,t_2)/e_{\sin}(k,t_1)]}{t_2-t_1}. \tag{9}$$

Due to the spatial discretization, the corresponding temporal growth rate $\omega_{i,\sin}(k)$ can be numerically determined in the range $-\pi/\delta x<k<\pi/\delta x$ in successive steps of size $\delta k=2\pi/L_x$.

In order to validate the above procedure, one checks the convergence of $\omega_{i,\sin}(k)$ for several $t_{1,2}$ values. It is also necessary to make sure that the corresponding eigenfunction,

$$\phi_{\sin}(k,y,t)=\frac{\hat{\omega}_{\sin}(k,y,t)}{e_{\sin}(k,t)}, \tag{10}$$

is indeed shape invariant in time.

2. Spatiotemporal instability, ray analysis

The spatiotemporal formulation is concerned with the determination of the Green's function, or equivalently, with the instability modes of given real group velocity v_g. It is thus necessary to investigate the wave packet structure in physical space, as these modes develop along the spatiotemporal ray $x/t=v_g$. This can be done unambiguously since the impulse response consists of a spatially oscillating wave

with a typical instability wavelength, smoothly modulated in space by an amplitude function (which is as smooth as desired provided that time t be taken sufficiently large). The perturbation spectrum then adopts a band structure that allows us to carry out the following procedure. First, the contribution of all Fourier modes with negative wave number $k<0$ is set to zero in spectral space in such a way that one recovers the usual complex exponential formulation. In physical space, the imaginary part associated to the real signal $\omega_{\sin}(x,y,t)$ is recovered by a spatial Hilbert transform along the streamwise x direction, as in Ref. 27:

$$\bar{\omega}_{\sin}(x,y,t)=\left(\delta(x)+\frac{i}{\pi x}\right)*\omega_{\sin}(x,y,t)$$

$$\equiv A_{\sin}(x,y,t)e^{i\varphi_{\sin}(x,y,t)}, \tag{11}$$

where $*$ designates the convolution operator in x, $A_{\sin}(x,y,t)$ the amplitude, and $\varphi_{\sin}(x,y,t)$ the phase within the wave packet.

The real amplitude function $A_{\sin}(x,t)$ of the dominant sinuous mode is obtained by integration along the cross-stream y direction according to the formula

$$A_{\sin}(x,t)=\left(\int_0^{L_y/2}A_{\sin}^2(x,y,t)dy\right)^{1/2}. \tag{12}$$

This quantity can be shown[31] to behave asymptotically as

$$A_{\sin}(x,t)\propto t^{-1/2}e^{\sigma_{\sin}(v_g)t}, \quad v_g=x/t=\text{const}, \quad t\to\infty. \tag{13}$$

In the above equation, $\sigma_{\sin}(v_g)$ designates the real growth rate of the sinuous mode dominating the dynamics along the ray $x/t=v_g$. It can be calculated as follows:

$$\sigma_{\sin}(v_g)\sim\frac{d}{dt}\ln[t^{1/2}A_{\sin}(v_gt,t)], \quad t\to\infty, \tag{14}$$

or, in discretized form,

$$\sigma_{\sin}(v_g)\approx\frac{\ln[A_{\sin}(v_gt_2,t_2)/A_{\sin}(v_gt_1,t_1)]}{t_2-t_1}+\sigma_0(t_1,t_2), \tag{15}$$

where the term

$$\sigma_0(t_1,t_2)=\frac{\ln(t_2/t_1)}{2(t_2-t_1)} \tag{16}$$

is a finite-time correction arising from the $t^{-1/2}$ factor in Eq. (13). For the values of t_1 and t_2 adopted in the following, $\sigma_0(t_1=36,t_2=40)\approx0.013$. This term was omitted in Ref. 28, thereby slightly underestimating the spatiotemporal growth rates without, however, affecting the results qualitatively. It has been included here, because its contribution as a constant is not negligible in relative magnitude, especially for nearly neutral modes.

At a given time t, the real part of the complex local wave number[32] $k_{r,\sin}$ can be evaluated on the x axis (at $y=0$) as follows:

$$k_{r,\sin}(x,t)=\frac{\partial\varphi_{\sin}}{\partial x}(x,0,t)=\mathcal{R}e\left\{\frac{1}{i\bar{\omega}_{\sin}}\frac{\partial\bar{\omega}_{\sin}}{\partial x}(x,0,t)\right\}. \tag{17}$$

The calculation of the derivative with respect to x in (17) is implemented in spectral space, where it reduces to a multiplication by ik. Asymptotically for large times, $k_{\sin}$ depends solely on the group velocity $v_g = x/t$.

Again, the validation of the above procedure involves a convergence check when using relations (15) and (17). The time invariance of the normalized eigenfunction,

$$\phi(v_g, y, t) = \frac{\omega_{\sin}(x = v_g t, y, t)}{A_{\sin}(x = v_g t, t) e^{i\varphi(x,0,t)}}, \tag{18}$$

must also be ensured.

C. Analysis of nonlinear simulations

Nonlinear effects, via the reintroduction of the term $\mathbf{u} \times \boldsymbol{\omega}$, have two consequences. On the one hand, this product displays a symmetry opposite to that of the sinuous modes, which thus forces a varicose contribution to the impulse response. On the other hand, it generates small wave numbers that destroy the previous band structure of the perturbation spectrum. In such cases, the Hilbert transform procedure (11) no longer leads to the retrieval of the wave packet envelope,[33] since it artificially expands the wave packet. In order to circumvent this difficulty, it is convenient to study the behavior of the rms local enstrophy $\eta(x,t)$ (hereafter simply called enstrophy) defined at each streamwise location x and time t by

$$\eta(x,t) = \left(\int_{-L_y/2}^{L_y/2} \omega^2(x,y,t)\,dy \right)^{1/2}. \tag{19}$$

This quantity satisfactorily accounts for the wave packet amplitude. [However, the carrier wave is thereby not fully filtered out. As a consequence, η curves generally exhibit wiggles (see Figs. 15, 17, and 20), which may provide some information on the wave packet phase.]

III. LINEAR IMPULSE RESPONSE

A. Strongly confined periodic wake ($L_y = 4.8$)

In the first simulation, the downstream and cross-stream sizes of the computational domain have, respectively, been selected to be $L_x = 102.4$ and $L_y = 4.8$. For such a strong confinement ($L_y/D = 2.4$), the periodic boundary conditions along y impose a strong coupling between adjacent wake images. The linear evolution of the initially localized disturbance (3) is computed up to time $t = 40$. The modal decomposition formulas (4)–(5) are applied to the perturbation field at several times during the simulation for both sinuous and varicose contributions. For the basic velocity profile under consideration (2), only the sinuous inviscid-like mode is found to be linearly unstable at the selected Reynolds number Re$=20$. In the following, we therefore focus solely on this dominant sinuous mode.

1. Temporal instability

The perturbation spectrum $e_{\sin}(k,t)$ extracted from the simulation is plotted in Fig. 4 at several times $t = 8,12,...,40$: temporal modes are seen to grow or decay exponentially according to the magnitude of the wave number.
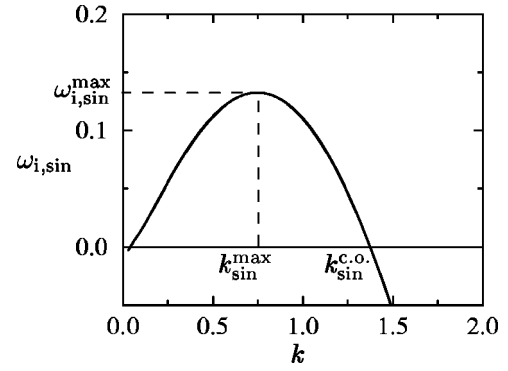

FIG. 5. The temporal growth rate $\omega_{i,\sin}$ of the sinuous mode, as determined from the wake impulse response for each Fourier component k at Re$=20$ and $L_y = 4.8$.

The corresponding sinuous mode growth rate $\omega_{i,\sin}$ is obtained through formula (9) applied between $t_1 = 36$ and $t_2 = 40$. The temporal growth rate $\omega_{i,\sin}$ is plotted as a function of wave number k in Fig. 5: the curve reaches its maximum value $\omega_{i,\sin}^{\max} = 0.132$ at wave number $k_{\sin}^{\max} = 0.750$. All modes with wave numbers larger than the ''cutoff'' wave number $k_{\sin}^{\text{c.o.}} = 1.374$ are damped.

2. Spatiotemporal instability

In order to determine the spatiotemporal instability properties of the flow, the physical perturbation vorticity field is observed on each spatiotemporal ray $x/t = \text{const} = v_g$. The evolution of the amplitude $A_{\sin}$ corrected by the factor $t^{1/2}$ [see Eq. (14)] is presented in Fig. 6 as a function of group velocity v_g. It can be seen that the set of amplitude curves exhibits two turning points, at v_- and v_+, indicating that the wave packet grows between two well-defined edges $x/t = v_-$ and $x/t = v_+$. The precise values of the edge velocities v_- and v_+ are determined by computing the corresponding growth rate $\sigma_{\sin}$ via formula (15), applied between $t_1 = 36$ and $t_2 = 40$. The spatiotemporal growth rate of the sinuous mode $\sigma_{\sin}$ is plotted in Fig. 7 as a function of group velocity v_g. The shape of the spatiotemporal growth-rate curve is very close to that of a parabola. The maximum $\sigma_{\sin}^{\max} = 0.132$ is observed along the ray $x/t = 0.51$. The maximum
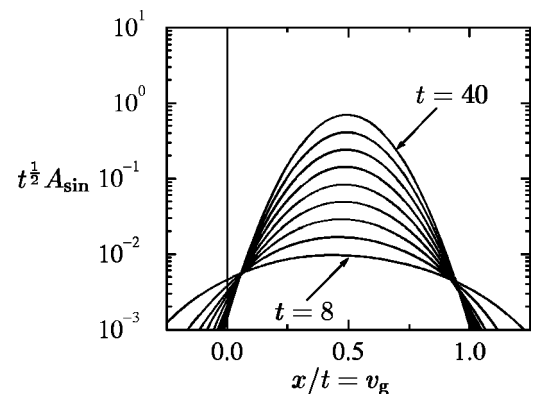

FIG. 6. Time-corrected amplitude $t^{1/2} A_{\sin}$ of the sinuous mode as a function of group velocity v_g at several times $t = 8,12,...,40$. The amplitude has been retrieved from the direct numerical simulation at Re$=20$ and $L_y = 4.8$.
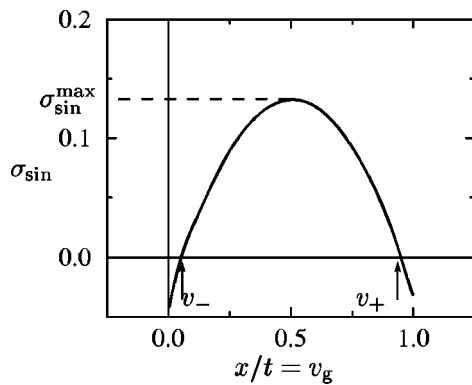
FIG. 7. The spatiotemporal growth rate $\sigma_{\sin}$ of the sinuous mode as determined from the results of Fig. 6 at Re=20 and L_y=4.8.

FIG. 9. The temporal growth rate $\omega_{i,\sin}$ of the sinuous mode, as determined from the wake impulse response for each Fourier component of wave number k at Re=20 and L_y=25.6. The dashed curve pertains to the case L_y =4.8, as plotted in Fig. 5.

value $\sigma_{\sin}^{\max}$ can be shown by construction[6] to coincide with the maximum temporal growth rate $\omega_{i,\sin}^{\max}$. The agreement between the two values determined numerically is seen to be better than 1%, and constitutes an internal coherence check for the method. The trailing and leading edges, which by definition sustain neutral waves, are the spatiotemporal rays $x/t=v_-=0.053$ and $x/t=v_+=0.95$. The growth-rate curve is almost symmetrical with respect to the central ray x/t =0.51. This feature can be explained by the fact that the cross-stream box size L_y=4.8 is close to the value L_y=2D =4 for which the basic flow velocity is invariant under the transformation $U\rightarrow1-U$, which would enforce the reflectional symmetry of the impulse response with respect to the ray $x/t=\frac{1}{2}$.

It is also possible to extract the streamwise wave number as a function of x/t via formula (17), as plotted in Fig. 8. The maximum amplification, obtained for $v_g=0.51$, is associated with the wave number value $k_{r,\sin}^{\max}=0.74$, in agreement with the value 0.75 previously obtained through the temporal approach. Furthermore, the wave number extracted by the Hilbert transform procedure was checked to coincide with direct wavelength measurements deduced from zero crossing of the perturbation vorticity along the symmetry x axis at time t =80 (Fig. 8).
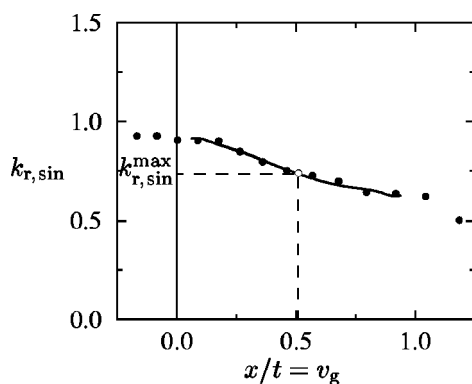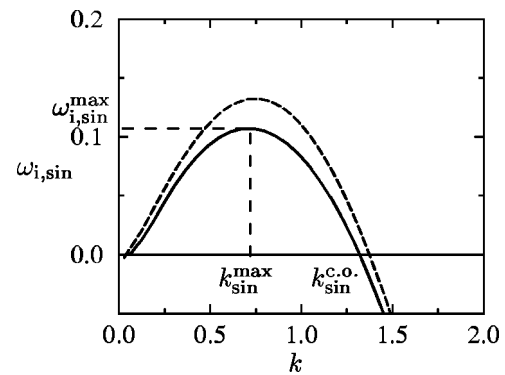
B. Weakly confined wake (L_y=25.6)

In order to simulate the dynamics of an isolated wake, the cross-stream box size was widened to L_y=25.6 (L_y/D =12.8). A linear simulation is performed in this wider domain for the same initial perturbation field (3) and Reynolds number Re=20 as for the confined case. The perturbation was checked to decay rapidly enough with $|y|$, so that at the boundaries $y=\pm L_y/2$ the velocity and the vorticity almost vanish. This check ascertained that y periodicity induced negligible coupling between adjacent wake images. The same decomposition and analysis procedure as in Sec. III A is applied. For the velocity profile (2) under study, only the sinuous mode is found to be unstable. The temporal growth rate $\omega_{i,\sin}(k)$ slightly differs from the case L_y=4.8, as displayed in Fig. 9, where both curves are plotted. The maximum growth rate is somewhat smaller, $\omega_{i,\sin}^{\max}=0.107$ at $k_{\sin}^{\max}$ =0.710. The cutoff wave number is reduced to $k_{\sin}^{\text{c.o.}}$ =1.320.

The linear growth rate on the spatiotemporal rays x/t =v_g determined with L_y=25.6 is compared to the curve obtained with L_y=4.8 (dashed line) in Fig. 10. The shape is still quasiparabolic, but the wave packet spatial extent is seen to be substantially reduced. Both trailing- and leading-edge
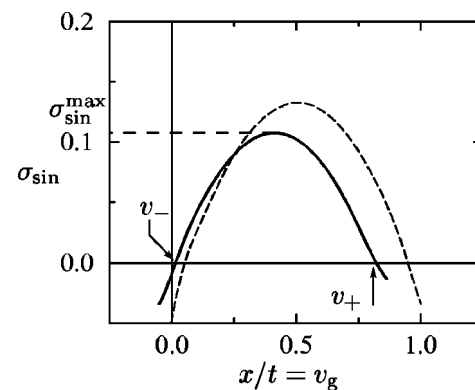
FIG. 8. The real part $k_{r,\sin}$ of streamwise wave number, as determined from the wake impulse response as a function of $x/t=v_g$ at t=40, Re=20, and L_y=4.8. —: extraction via formula (17); ●: direct measurement on the vorticity field.

FIG. 10. The spatiotemporal growth rate $\sigma_{\sin}$ of the sinuous mode, as determined from the wake impulse response on each spatiotemporal ray x/t =v_g at Re=20 and L_y=25.6. The dashed curve pertains to the case L_y =4.8, as plotted in Fig. 7.

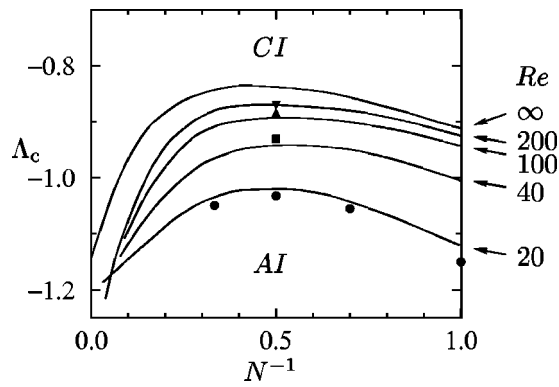FIG. 11. Critical values of the velocity ratio Λ_c for convective/absolute transition, for different values of N and Re. The continuous lines taken from the study by Monkewitz,[7] Fig. 4, are obtained by saddle-point tracking. The symbols denote critical Λ_c values deduced from the trailing edge velocities v_- obtained by DNS for Re=20($\bullet$), Re=40($\blacksquare$), Re=100($\blacktriangle$), and Re =200($\blacktriangledown$).

FIG. 12. The real part $k_{r,\text{sin}}$ of streamwise wave number as determined from the wake impulse response as a function of $x/t = v_g$ at $t=40$, Re=20 for $L_y=25.6$.—: extraction via formula (17); $\bullet$: direct measurement on the vorticity field.

velocities, respectively, decrease to $v_-=0.016$ and $v_+=0.82$. It is surprising that in spite of the fact that the mean basic velocity is larger in the case $L_y=25.6$ than in the case $L_y=4.8$, group velocities have globally decreased. In particular, the trailing-edge velocity has decreased, thus promoting the absolute character of the instability. The ray $x/t=\frac{1}{2}$ is no longer a symmetry axis for the curve, as the invariance under the transformation $U\rightarrow 1-U$ no longer holds. Besides, the weakly confined wake is less unstable than the strongly confined one, since $\sigma_{\text{sin}}^{\max}=0.107$ instead of 0.132.

The value of the trailing-edge velocity v_- can be compared with the result obtained by Monkewitz[7] by direct application of the Briggs–Bers criterion[34] on the viscous dispersion relation. From his Fig. 4, a critical velocity ratio for the occurrence of absolute instability is $\Lambda_c^{(M)}=-1.02$. The relationship between the present v_- value and Λ_c is given by $\Lambda_c=(2v_- -1)^{-1}$, which in our case yields $\Lambda_c=-1.03$. This Λ_c value only differs by 1% from $\Lambda_c^{(M)}$. The present method of investigation has been further validated by similar comparisons for different values of N and Re. The data obtained for $N=2$, Re=20, 40, 100, 200 and for Re=20, $N=1, 1.4, 2, 3$ have been superposed on the results obtained by Monkewitz in Fig. 11. In all cases, a satisfactory agreement is obtained. This confirms the validity and efficiency of the present procedure based on direct numerical simulations. It also confirms the convergence of the method, as well as the negligible effects of finite-time approximation and finite box size, particularly in the cross-stream direction.

The most important difference between the linear instability properties of the weakly and strongly confined wakes arises from the real part $k_{r,\text{sin}}$ of the wave number, as represented in Fig. 12. Near the leading edge $v_+=0.82$, the wavelength is seen to diverge—although, strictly speaking, the Hilbert transform procedure fails to separate phase and amplitude near such points. The oscillatory behavior of the wave packet ends near the leading edge, thus forbidding the formation of new vortices feeding the wave packet from downstream.
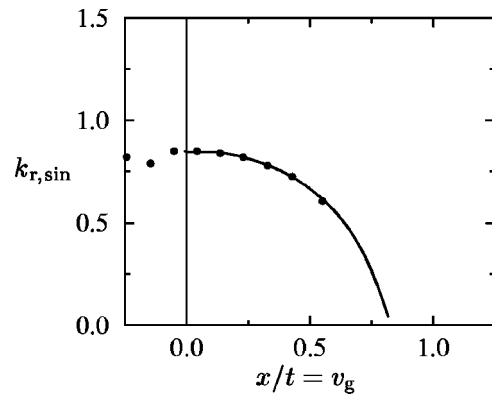
IV. NONLINEAR IMPULSE RESPONSE

Nonlinear simulations have been performed in each of the above cases for the same initial condition (3). The nonlinear term $\mathbf{u}\times\boldsymbol{\omega}$, now included, causes the wave packet to saturate after an initial exponential growth. The influence of the saturation on the edge dynamics is investigated successively in both configurations, $L_y=4.8$ and $L_y=25.6$. The nonlinear term also breaks the symmetry $y\rightarrow -y$ and sinuous and varicose modes cannot be treated separately. More precisely, a varicose wave packet exists, but the sinuous wave packet also generates a varicose perturbation.

A. Strongly confined periodic wake ($L_y=4.8$)

The nonlinear evolution of an initially localized perturbation in the strongly confined wake ($L_y=4.8$) has been simulated at the same Reynolds number Re=20 up to time $t=80$. Isocontours of the total vorticity $\Omega(y)+\omega(x,y,t)$ are plotted in Fig. 13 at several times. Note that in the streamwise x direction, only the central region of the domain has been represented. The initial pulse is merely visible on the bottom graph at $x=0$. The perturbation both increases in amplitude and develops in space, as may be seen from the oscillations of the isocontours. Near $t=40$, the oscillations reach the amplitude of the basic flow, and vorticity begins to roll up into counter-rotating vortices. For $t\geqslant 60$, several wavelengths of a quasiregular pattern can be distinguished, the number of which increases as the wave packet spreads out along the streamwise x direction. The time evolution of the rms perturbation vorticity over the entire domain,

$$\varpi(t)=\left(\int\int \omega^2(x,y,t)dxdy\right)^{1/2}, \qquad (20)$$

is presented in Fig. 14. After a transient period ($t<10$), the perturbation undergoes an exponential growth ($10<t<35$). During both periods, the system evolution is governed by linear instability mechanisms, and the curve $\varpi(t)$ follows the dashed curve obtained in the linear simulation presented in Sec. III A. The wave packet then undergoes a saturation process ($35<t<55$), during which the energy growth is sub-
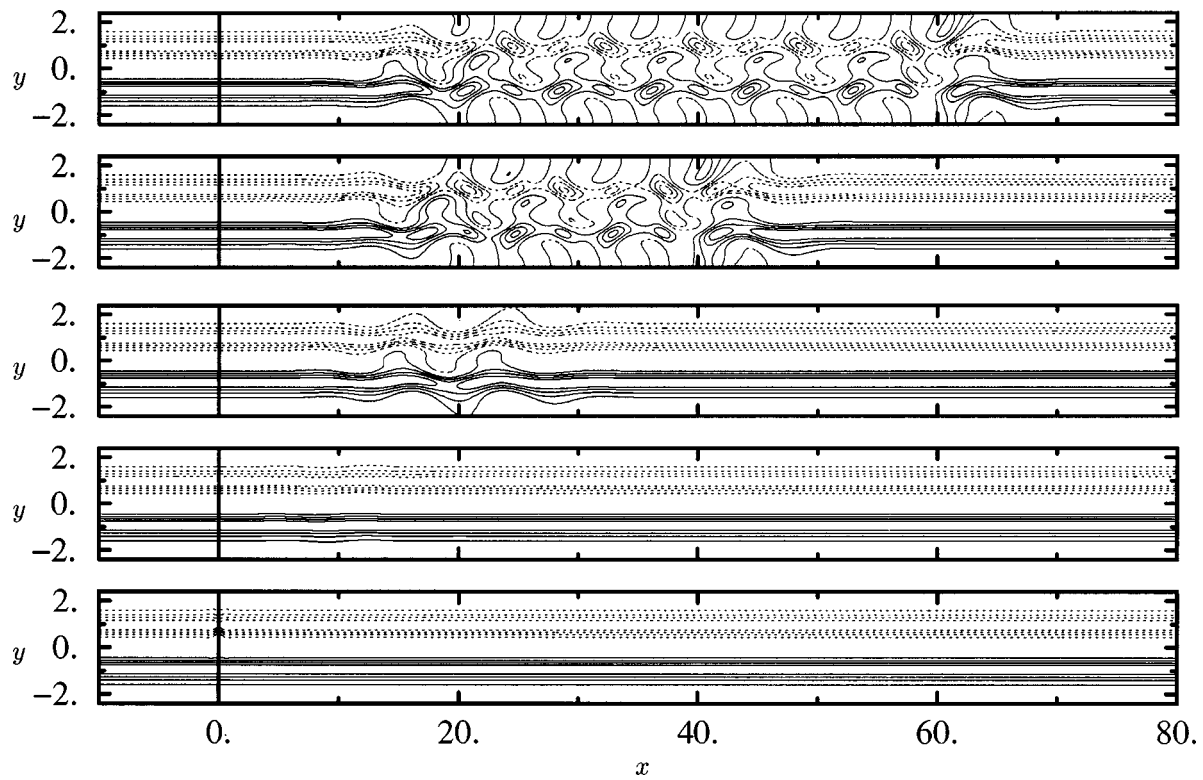
FIG. 13. Isocontours of the total vorticity distribution $\Omega(y) + \omega(x,y,t)$ at several times $t=0$, 20, 40, 60, and 80 (from bottom to top) for Re=20 and L_y =4.8. Solid isolines pertain to positive levels 0.25, 0.5, 0.75, and 1. Dotted isolines pertain to negative levels -0.25, -0.5, -0.75, and -1. The computational domain has been cropped to a shorter streamwise extent $-10 \leqslant x \leqslant 80$ (for the original domain, $-20 \leqslant x \leqslant 184.8$).

stantially reduced. Eventually, ϖ grows linearly as a function of time while the saturated wave packet spreads out at the constant extension rate $v_+^{NL} - v_-^{NL}$.

This saturation process may also be followed on the waterfall plot of Fig. 15, where the rms enstrophy η is plotted as a function of x at several times. The wave packet spreading is clearly seen on the seven top curves. The two edges delimiting the wave packet in Fig. 15 have been determined by following the constant η levels prevailing at the linear stage ($t \leqslant 35$). It can be observed that, in the nonlinear régime ($t>35$), the propagation of the two edges seems unaffected by the wave packet amplitude saturation. The $x-t$ diagram of Fig. 16 displays the paths along which the centerline vorticity $\omega(x,0,t)$ vanishes, i.e., along which the wave

packet phase $\varphi(x,y=0,t)$ is constant (and from one line to the next alternatively equals 0 and π). (As the antisymmetric part of the perturbation vorticity vanishes on the centerline, this procedure provides information on the sole symmetric part, i.e., the sinuous component.) Within the wave packet, the phase velocity is seen to lie between the two front velocities. As a consequence, new vortices form at the trailing edge, *but also* at the leading edge of the wave packet.

In order to examine precisely the effect of nonlinear terms on the wave packet edges, the enstrophy curves $\eta(x,t=80)$ obtained by linear and nonlinear simulations at $t=80$ are superposed in Fig. 17. The comparison of the two
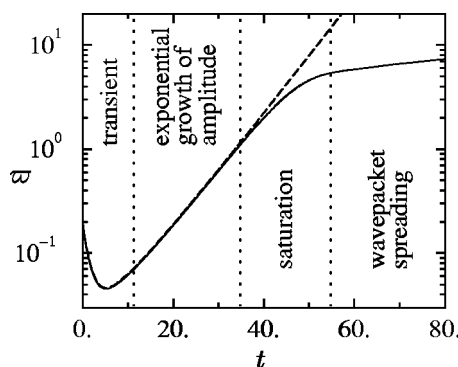

FIG. 14. Temporal evolution of the rms perturbation vorticity ϖ for Re =20 and L_y=4.8.
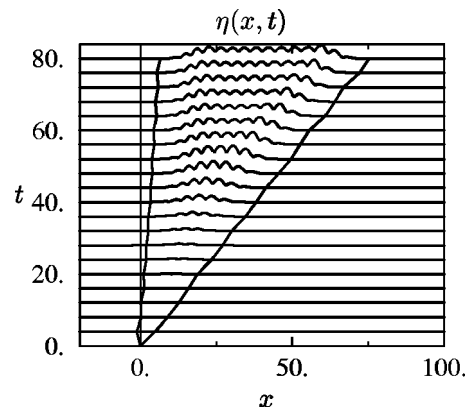

FIG. 15. Waterfall plot of enstrophy η in the x-t plane at Re=20 and L_y =4.8. The wave packet edges are also represented.
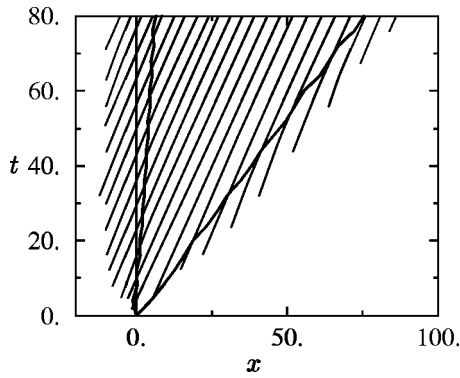
FIG. 16. The spatiotemporal $x-t$ diagram presenting the isophase paths along which $\varphi(x,y=0,t)=0,\pi$, at Re=20 and $L_y=4.8$. Bold lines represent wave packet edges.

curves clearly demonstrates that both amplitude and phase obtained by linear and nonlinear simulations coincide accurately on each wave packet edge over more than four enstrophy decades. This situation corresponds remarkably to scenarios (a)–(b) in Fig. 3. The nonlinear terms just cause the amplitude to saturate in the wave packet core, while the phase is left unchanged from linear to nonlinear simulations, as could also be checked by direct comparison of the 2-D vorticity fields. As a consequence, both front velocities $v_\pm^{\mathrm{NL}}$ are seen to be purely enforced by the linear instability properties of the medium. For the strongly confined periodic parallel wake, the linear front-velocity selection of Dee and Langer[23] holds:

$$v_\pm^{\mathrm{NL}}=v_\pm . \tag{21}$$

Consequently, the convective/absolute nature of this flow is preserved from the linear to nonlinear régime.

B. Weakly confined wake ($L_y=25.6$)

Isocontours of the total vorticity field $\Omega(y)+\omega(x,y,t)$, obtained in the nonlinear simulation for the weakly confined wake at $L_y=25.6$, are displayed in Fig. 18 at several times. Only the central region of the computational domain in x and y has been represented. As in the experiment of Le Gal and
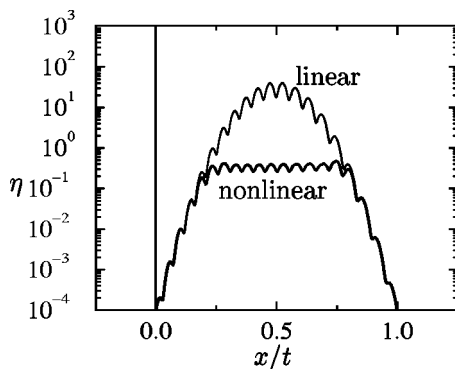

FIG. 17. Enstrophy distribution as a function of x/t at time $t=80$ for linear (thin curve) and nonlinear (bold curve) simulations at Re=20 and $L_y=4.8$.

Croquette,[18] passive tracer particles have been regularly spaced on the x axis at $t=0$, and their evolution is followed by implementing a predictor/corrector algorithm. As seen from the plot at $t=80$ in Fig. 18, the separation of the initial line into small parts under the effect of rollup is evident, as in Fig. 2. One should note, however, that contrary to experiments, the present wake profile is independent of the streamwise x direction. Possibly as a consequence of this fact, the wave packet is found to be far less regular than its experimental counterpart of Fig. 2, and the vortex street eventually becomes disorganized for large times, as can be seen in the neighborhood of the downstream front at $t=100$ in Fig. 18.

The spatiotemporal $x-t$ diagram of Fig. 19 confirms the existence of an instability in the saturated region. In this isophase representation, a vortex merging event corresponds to the loss of one wavelength, and appears as the annihilation of two adjacent lines. Such a vortex merging is seen to take place at $t\approx100$ (arrow C). Note that, contrary to what happens in the strongly confined wake, no additional wavelength is created from the downstream side through the leading front of the wave packet. This feature is also observed in the experiment of Fig. 2: the wave packet ends abruptly in a fully developed vortex, which remains the same during the entire observation time. The steepness of the leading front is no nonlinear effect, but can be accounted for by linear considerations: as the linear wavelength becomes infinite at the leading edge (see Fig. 12), phase velocity c and group velocity v_g tend to coincide since

$$c\equiv\frac{\omega}{k}\rightarrow\frac{\partial\omega}{\partial k}=v_g, \quad \text{when} \quad \omega,k\rightarrow0 \quad \text{and} \quad c\neq0. \tag{22}$$

This relation prevents the creation of new vortices at the leading edge where isophase lines become parallel to the edge.

In Fig. 19, the edges have been determined as previously. In the nonlinear régime ($t>60$), the leading edge seems to depart from its linear counterpart. This phenomenon is analyzed by comparison of the enstrophy distribution curves $\eta(x,t=80)$ obtained from linear and nonlinear simulations [Fig. 20(a)]. Figure 20(a) reveals three main differences with respect to the case $L_y=4.8$, as indicated by the three arrows. A vortex-merging event can be spotted by the irregularity of the enstrophy curve (indicated by arrow C). Moreover, both nonlinear fronts are seen to differ from linear ones (arrows A and B) because of enstrophy excesses present at both wave packet ends. These enstrophy excesses have both been observed to consist of zero-wave number perturbations, but their symmetry differ. The perturbation at the leading edge (arrow B) displays the symmetry opposite to that of the basic flow: it consists of a slight shift of the shear layers. By contrast, the perturbation at the trailing edge (arrow A) has the same symmetry as the basic flow: it consists of a slight pinching of the basic wake.

It is of interest to further investigate the "sinuous" contribution to the wave packet, which is known to give rise to the alternating vortices typical of the von Kármán street. The "sinuous" enstrophy computed by formula (19), where ω is replaced by ω_{sin} is plotted in Fig. 20(b). From the compari-
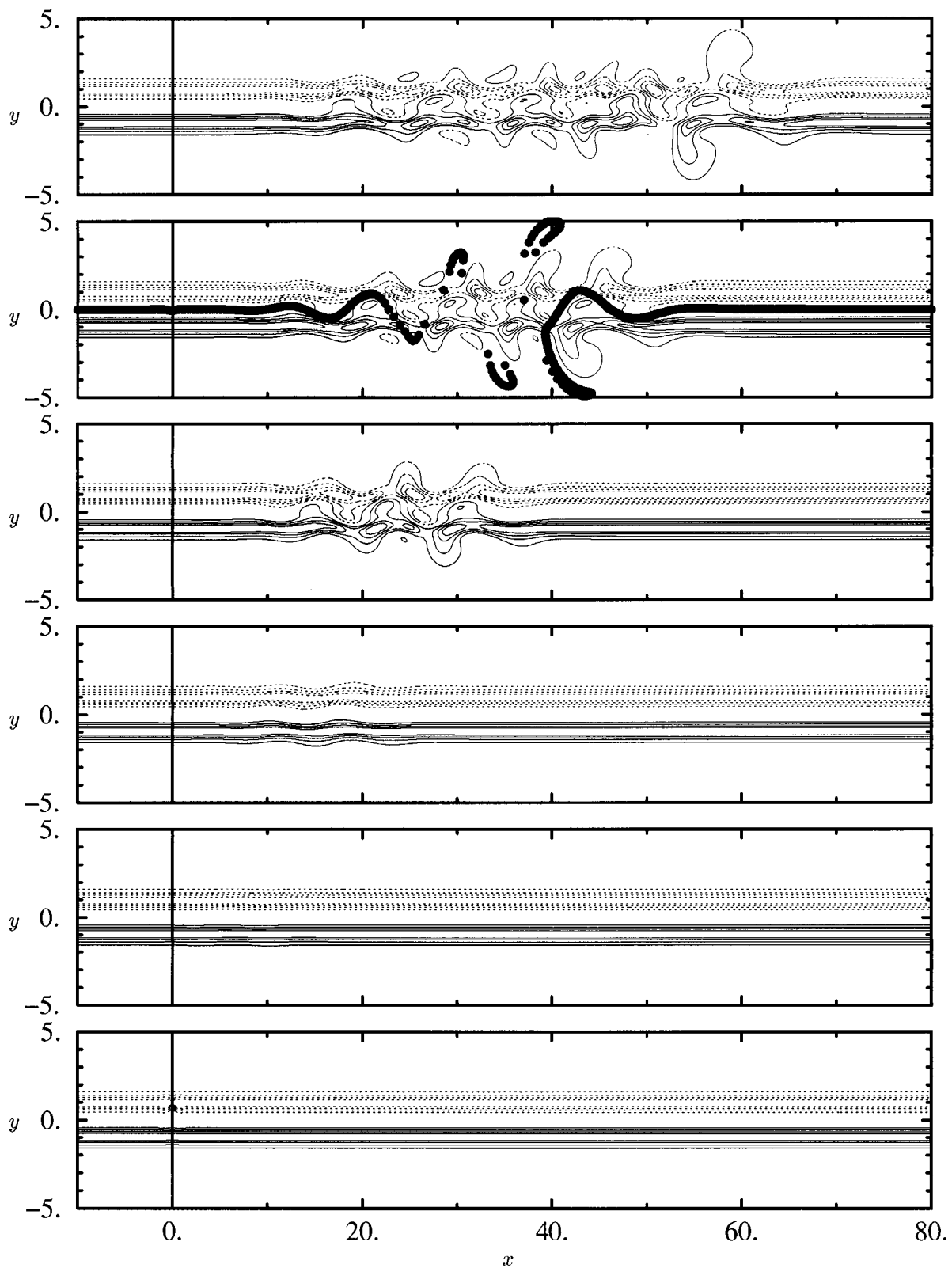
FIG. 18. Isocontours of the total vorticity distribution $\Omega(y)+\omega(x,y,t)$ at several times $t=0$, 20, 40, 60, 80, and 100 for Re=20 and $L_y=25.6$. Solid isolines pertain to positive levels 0.25, 0.5, 0.75, and 1. Dotted isolines pertain to negative levels -0.25, -0.5, -0.75, and -1. The computational domain has been cropped to shorter streamwise and crosswise extents $-10\leqslant x\leqslant80$ and $-5\leqslant y\leqslant5$ (for the original domain, $-20\leqslant x\leqslant184.8$ and $-12.8\leqslant y\leqslant12.8$). For $t=80$, the dispersion of passive tracer particles initially equispaced on the centerline has been represented.

son with the enstrophy curve obtained from the linear simulation, also plotted, it is clear that the trailing front of the "sinuous" part of the wave packet (the "vortex front") is linearly selected, as both linear and nonlinear curves now

strictly superpose at the trailing edge. This is also clearly seen in Fig. 19, where the vortex front represented by a dashed line exhibits a constant slope. This feature indicates that linear front-velocity selection $v_-=v_-^{\mathrm{NL}}$ holds when the
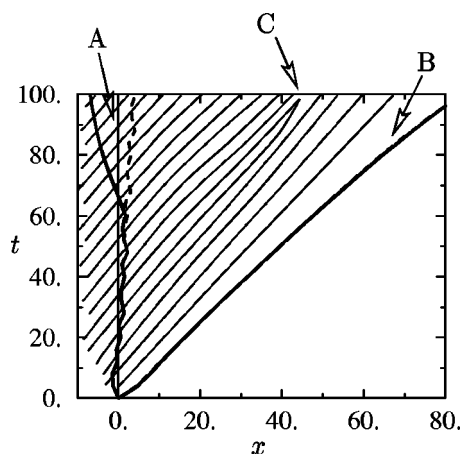
FIG. 19. Spatiotemporal $x-t$ diagram of isophase lines $\varphi(x,y=0,t)$ $=0,\pi$. The wave packet edges are represented in bold (solid line: full wave packet; dashed line: ''sinuous'' component only). Arrows A and B point to the regions analyzed in Fig. 20. Arrow C points to the merging event.

sole sinuous contribution is considered. The upstream vortex front then follows the linear selection mechanism, even though the vortex street downstream of its displays strong nonlinearities, and though it is itself unstable and susceptible to merging events.

V. CONCLUDING REMARKS

The linear and nonlinear impulse response of parallel wake flows has been investigated by direct numerical simulation. In the case of a strongly confined periodic wake, it has been shown by direct comparison of the linear and nonlinear wave packet evolution that the upstream and downstream

FIG. 20. (a) Enstrophy η and (b) the ''sinuous'' part η_{sin} of enstrophy distributions as a function of x/t at time $t=80$ for linear (thin curves) and nonlinear (bold curves) simulations at Re=20 and $L_y=25.6$.

fronts are both linearly selected, according to the Dee and Langer[23] mechanism. In the case of a weakly confined wake, the wave packet dynamics were found to be affected by long-wavelength perturbations and instabilities. However, the upstream *vortex front*, isolated by considering the ''sinuous'' component of the wave packet only, was shown to be linearly selected. In that case, the vortex street was observed to be irregular and unstable to vortex merging. The drastic reduction of the cross-stream box size to $L_y=4.8$ effectively quenched the pairing instability and a regular stable vortex street was obtained. This study has presented the case of a system governed by the Navier–Stokes equations, which is highly unstable toward infinitesimal perturbations, and from which a stable saturated state arises in the form of a fully developed vortex street. The present configuration is the analog for a real flow of the idealized front dynamics investigated until now in the context of amplitude evolution equations.[21,22,19,35,14] Nonlinear terms are found to limit the amplitude at some saturation level in the wave packet core, but have no effect on the wave packet propagation. The front-velocity selection is thus linear for both leading and trailing edges.

In the case of a weakly confined parallel wake, the situation is somewhat complicated by the vortex-street instability. The existence of a well-defined front traveling at constant velocity is *a priori* not expected in that case. Indeed, a zero-wave number deformation (antisymmetric in vorticity) of the upstream front is observed, which does not seem to be linked directly to a vortex-pairing process. This deformation was checked not to depend on the grid step δx and cannot be attributed to a numerical artifact. It is likely that, in a realistic configuration, the presence of the bluffbody would suppress this deformation. Thus, it seems plausible to base the ''vortex'' front velocity on the sinuous component of the wave packet. The application of the procedure shows that the vortex-front velocity is linearly selected also in the weakly confined configuration. Under these restrictions, the linear convective/absolute instability threshold corresponds to the nonlinear convective/absolute instability threshold.

The linear front-velocity selection has been found to take place for *all* values of N and Re (see Sec. III B), pertaining to far-wake ($N=1,1.4$) as well as near-wake ($N=2,3$) basic profiles and covering a relatively large range of advection levels. Therefore, in the family of profiles (2), the linear convective/absolute transition should coincide with the non-linear one. Linear spatiotemporal instability properties have been recently shown[16] to successfully predict transition in nonparallel flows such as wakes. Although the present study is restricted to parallel flow instability, we conjecture that it explains this success qualitatively, as nonlinear effects do not affect the absolute instability threshold.

Front dynamics has previously been investigated in Taylor–Couette[1] and Rayleigh–Bénard[2] systems with a small superimposed throughflow. In such weakly nonlinear cases, an amplitude equation approach is legitimate, and one expects to recover the front-velocity selection criterion proposed by Dee and Langer.[23] In the present study, conducted for a shear flow far away from the onset of instability, the
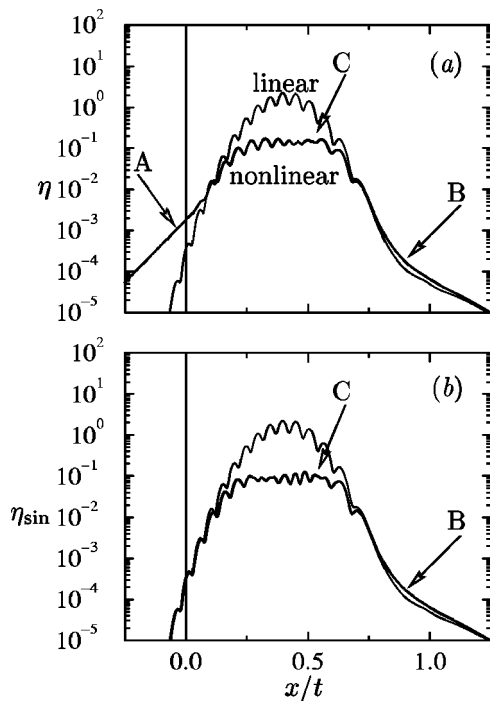
same selection criterion has been shown to hold, although strongly nonlinear mechanisms have been activated.

ACKNOWLEDGMENTS

[1]P. Büchel, M. Lücke, D. Roth, and R. Schmitz, ''Pattern selection in the absolutely unstable regime as a nonlinear eigenvalue problem: Taylor vortices in axial flow,'' Phys. Rev. E **53**, 4764 (1996).

[2]J. Fineberg and V. Steinberg, ''Vortex-front propagation in Rayleigh–Bénard convection,'' Phys. Rev. Lett. **58**, 1332 (1997).

[3]P. A. Monkewitz and K. D. Sohn, ''Absolute instability in hot jets,'' AIAA J. **26**, 911 (1988).

[4]S. Jendoubi and P. J. Strykowski, ''Absolute and convective instability of axisymmetric jets with external flow,'' Phys. Fluids **6**, 3000 (1994).

[5]C. Mathis, M. Provansal, and L. Boyer, ''The Bénard–von Kármán instability: An experimental study near the threshold,'' J. Phys. Lett. (France) **45**, L483 (1984); M. Provansal, C. Mathis, and L. Boyer, ''Bénard–von Kármán instability: transient and forced regimes,'' J. Fluid Mech. **182**, 1 (1987).

[6]P. Huerre and P. A. Monkewitz, ''Local and global instabilities in spatially developing flows,'' Annu. Rev. Fluid Mech. **22**, 473 (1990).

[7]P. A. Monkewitz, ''The absolute and convective nature of instability in two-dimensional wakes at low Reynolds numbers,'' Phys. Fluids **31**, 999 (1988).

[8]K. Hannemann and H. Oertel, Jr., ''Numerical simulation of the absolutely and convectively unstable wake,'' J. Fluid Mech. **199**, 55 (1989).

[9]R. T. Pierrehumbert, ''Local and global baroclinic instability of zonally varying flow,'' J. Atmos. Sci. **41**, 2141 (1984).

[10]W. Koch, ''Local instability characteristics and frequency determination of self-excited wake flows,'' J. Sound Vib. **99**, 53 (1985).

[11]P. A. Monkewitz and L. N. Nguyen, ''Absolute instability in the near-wake of two-dimensional bluff bodies,'' J. Fluids Struct. **1**, 165 (1987).

[12]J.-M. Chomaz, P. Huerre, and L. G. Redekopp, ''Bifurcations to local and global modes in spatially developing flows,'' Phys. Rev. Lett. **60**, 25 (1988).

[13]S. Le Dizès, P. Huerre, J.-M. Chomaz, and P. A. Monkewitz, ''Linear global modes in spatially developing media,'' Philos. Trans. R. Soc. London, Ser. A **354**, 169 (1996).

[14]B. Pier, P. Huerre, J.-M. Chomaz, and A. Couairon, ''Selection criteria for soft and steep nonlinear global modes in spatially developing media,'' to appear in Phys. Fluids.

[15]M. Schumm, E. Berger, and P. A. Monkewitz, ''Self-excited oscillations in the wake of two-dimensional bluff bodies and their control,'' J. Fluid Mech. **271**, 17 (1994).

[16]D. A. Hammond and L. G. Redekopp, ''Global dynamics of symmetric and asymmetric wakes,'' J. Fluid Mech. **331**, 231 (1997).

[17]P. A. Monkewitz, P. Huerre, and J.-M. Chomaz, ''Global linear stability analysis of weakly non-parallel shear flows,'' J. Fluid Mech. **251**, 1 (1993).

[18]P. Le Gal and V. Croquette, ''Analyse en temps réel d'un sillage,'' Congrès SFP 1991, Caen, France, Bull. SFP, 1991, Vol. 81, p. 29.

[19]J.-M. Chomaz, ''Absolute and convective instabilities in nonlinear systems,'' Phys. Rev. Lett. **69**, 1931 (1992).

[20]A. Kolmogorov, I. Petrovsky, and N. Piskunov, ''Investigation of a diffusion equation connected to the growth of materials, and application to a problem in biology,'' *Bulletin de l'université d'état à Moscou, Série internationale, Section A, Vol. 1, 1937*, in Selected works of A. N. Kolmogorov, edited by V. M. Tikhomirov (Kluwer Academic, New York, 1991).

[21]W. van Saarloos, ''Front propagation into unstable states: Marginal stability as a dynamical mechanism for velocity selection,'' Phys. Rev. A **37**, 211 (1988).

[22]W. van Saarloos, ''Front propagation into unstable states. II. Linear versus nonlinear marginal stability and rate of convergence,'' Phys. Rev. A **39**, 6367 (1989).

[23]G. Dee and J. S. Langer, ''Propagating pattern selection,'' Phys. Rev. Lett. **50**, 383 (1983).

[24]A. Hanna, A. Saul, and K. Showalter, ''Detailed studies of propagating fronts in the iodate oxidation of arsenous acid,'' J. Am. Chem. Soc. **104**, 3838 (1982).

[25]P. Palffy-Muhoray, H. J. Yuan, B. J. Frisken, and W. van Saarloos, in *Nonlinear Evolution of Spatio-temporal Structures in Dissipative Continuous Systems*, edited by F. H. Busse and L. Kramer (Plenum, New York, 1990).

[26]A. Vincent and M. Meneguzzi, ''The spatial structure and statistical properties of homogeneous turbulence,'' J. Fluid Mech. **225**, 1 (1991).

[27]P. Brancher and J.-M. Chomaz, ''Absolute and convective secondary instabilities in spatially periodic shear flows,'' Phys. Rev. Lett. **78**, 658 (1997); P. Brancher, ''Étude numérique des instabilités secondaires de jets,'' Ph.D. thesis, École Polytechnique, France, 1996.

[28]I. Delbende, J.-M. Chomaz, and P. Huerre, ''Absolute/convective instabilities in the Batchelor vortex: a numerical study of the linear impulse response,'' J. Fluid Mech. **355**, 229 (1998).

[29]J. Delfs, J. Ehrhard, E. Meiburg, and H. Örtel, Jr., ''Lagrange identification of absolutely unstable regimes in wakes,'' Acta Mech. **122**, 89 (1997).

[30]P. G. Drazin and W. H. Reid, *Hydrodynamic Stability* (Cambridge University Press, Cambridge, 1981).

[31]P. Huerre and P. A. Monkewitz, ''Absolute and convective instabilities in free shear layers,'' J. Fluid Mech. **159**, 151 (1985).

[32]G. B. Whitham, *Linear and Nonlinear Waves* (Wiley, New York, 1974).

[33]W. K. Melville, ''Wave modulation and breakdown,'' J. Fluid Mech. **128**, 489 (1983).

[34]R. J. Briggs, *Electron–Stream Interaction With Plasmas* (MIT Press, Cambridge, MA, 1964); A. Bers, ''Linear waves and instabilities,'' in *Physique des Plasmas*, edited by C. deWitt and J. Peyraud (Gordon & Breach, New York, 1975), pp. 117–215.

[35]A. Couairon and J.-M. Chomaz, ''Global instability in fully nonlinear systems,'' Phys. Rev. Lett. **77**, 4015 (1996); A. Couairon, ''Modes globaux fortement non-linéaires dans les écoulements ouverts,'' Ph.D. thesis, École Polytechnique, France, 1997.